

Physics-Based Modeling of GaN HEMTs

Stanislav Vitinov, Vassil Palankovski, Stephan Maroldt, Rüdiger Quay,
Saad Murad, Thomas Rödle, and Siegfried Selberherr, *Fellow, IEEE*

Abstract—A thorough approach to the investigation of GaN-based high-electron mobility transistors by device simulation is demonstrated. Due to structure and material peculiarities, new comprehensive hydrodynamic models for the electron mobility are developed and calibrated. Relying on this setup, three different independent device technologies are simulated and compared. We further study the pronounced decrease in the transconductance g_m at higher gate bias. We show that the electric field distribution and the resulting carrier velocity quasi-saturation are the main source for the transconductance collapse.

Index Terms—Gallium compounds, HEMTs, semiconductor device modeling, simulation software.

I. INTRODUCTION

WIDE bandgap GaN-based high-electron mobility transistors (HEMTs) exhibit power properties that make them eligible for use in radio-frequency applications. Focused extensive investigations in recent years have solved various technology issues and vastly improved the device performance [1], [2]. Nowadays, AlGaIn/GaN HEMTs have entered mass production. Other device concepts based on a GaN-channel as well are showing promising results too [3], [4]. However, there is still place for improvement and optimization: a better understanding of g_m collapse at higher gate-source voltages can be useful to counter g_m degradation and thus linearity reduction. As the derivatives of the transconductance with respect to the gate voltage are detrimental to intermodulation distortion [5], [6], a profound knowledge of the causes for the

transconductance nonlinearity significantly helps the selection of a proper load resistance. Therefore, in order to further study, optimize, and down scale the structures, a reliable simulation tool is very helpful.

Models that account for the specific physics in a given semiconductor material are crucial for device modeling. While for silicon there exist well-established models, the GaN system still poses certain challenges. The major one is caused by the negative differential electron mobility (NDM) predicted by Monte Carlo (MC) simulations, e.g., [7] and [8]. Several works provide direct evidences of this effect: a peak velocity at 191 kV/cm in lightly doped material was first reported in [9]; however, later studies observed a velocity saturation and consequent decrease at around 225 kV/cm [10]. Whereas the latter measurement was in normal plane, measurements in basal plane yielded saturation velocity at 180 kV/cm in n -type GaN and at 140 kV/cm in AlGaIn/GaN heterostructures [11]. Indirect evidence of NDM in GaN such as transferred-electron effects in Gunn diodes also exist [12]. Nevertheless, a definite examination of the problem is still pending since not only are the saturation velocities reported by different groups contradicting (largely depending on the material quality and orientation) but also there is still no agreement on the reason for the NDM (intervalley transfer or nonparabolicity of the conduction band). Therefore, a model for GaN has to be capable of describing NDM effects while providing some straightforward approach to fine tuning the velocity-field characteristics as the latter has been found to be detrimental to transconductance collapse phenomena [13], [14].

Several groups have proposed various models and model parameter sets for the simulation of GaN-based devices. Farahmand *et al.* provide a low-field electron mobility model that accounts for temperature and the ionized impurity concentrations, as well as a high-field mobility model, based on MC simulation results [15]. Another low-field model, which is valid in a large temperature and concentration range, is proposed by Mnatsakanov *et al.* [16]. A highly parameterized field-dependent model based on an extensive data pool is developed by Schwierz [17]. Turin proposed another high-field model that delivers excellent agreement with the results from MC simulations [18]. All those models are suited only for the drift-diffusion (DD) transport model. However, the latter is not able to deliver accurate results for sub-halfmicrometer devices [19]; therefore, a hydrodynamic (HD) transport model is essential, particularly for small-signal AC analysis. In this paper, we propose two models specific to the HD simulation of GaN-based devices. Special care is taken of the consistency between the HD and DD models. They are calibrated and implemented in our two-dimensional device simulator MINIMOS-NT [20], which has proven to be a suitable tool for the analysis of

Manuscript received September 29, 2011; revised November 30, 2011; accepted December 2, 2011. Date of publication January 27, 2012; date of current version February 23, 2012. This work was supported by the Austrian Science Fund (FWF) under START Project Y247-N13. The review of this paper was arranged by Editor G. Ghione.

S. Vitinov was with the Advanced Materials and Device Analysis Group, Institut für Mikroelektronik, Technische Universität Wien, 1040 Vienna, Austria. He is now with Infineon Technologies, 9500 Villach, Austria (e-mail: vitinov@iue.tuwien.ac.at).

V. Palankovski is with the Advanced Materials and Device Analysis Group, Institut für Mikroelektronik, Technische Universität Wien, 1040 Vienna, Austria (e-mail: palankovski@iue.tuwien.ac.at).

S. Murad was with NXP Semiconductors, 6534 Nijmegen, The Netherlands. He is now with Azzuro Semiconductors, 39104 Magdeburg, Germany (e-mail: saad.murad@nxp.com).

T. Rödle is with NXP Semiconductors, 6534 Nijmegen, The Netherlands (e-mail: thomas.roedle@nxp.com).

S. Maroldt and R. Quay are with the Fraunhofer Institute for Applied Solid-State Physics, 79108 Freiburg, Germany (e-mail: stephan.maroldt@iaf.fraunhofer.de; ruediger.quay@iaf.fraunhofer.de).

S. Selberherr is with the Institut für Mikroelektronik, Technische Universität Wien, 1040 Vienna, Austria (e-mail: selberherr@iue.tuwien.ac.at).

Color versions of one or more of the figures in this paper are available online at <http://ieeexplore.ieee.org>.

Digital Object Identifier 10.1109/TED.2011.2179118

TABLE I
LOW-FIELD MOBILITY PARAMETERS

| μ_{300}^L | μ_{300}^{\min} | C_{300}^{ref} | α | γ_0 | γ_1 | γ_2 |
|--------------------------|-------------------------|-------------------------------------|----------|------------|------------|------------|
| 1600 cm ² /Vs | 100 cm ² /Vs | 3×10^{17} cm ⁻³ | 0.7 | 1.3 | -1.5 | -0.2 |

heterostructure devices [21], [22]. This approach offers a very time-efficient solution (compared with MC simulations), which is well suited for optimization problems.

Using the same calibrated setup, we simulate three different generations of AlGaIn/GaN HEMTs. Excellent accuracy for the DC and AC characteristics in comparison with measurement results is achieved. We also study the electron transport in the extrinsic and intrinsic regions in a wide range of gate voltages. We show that the transconductance decrease should not be attributed to negative differential mobility effects and is also reproducible by using velocity-field characteristics conform to MC results.

II. MODELS AND CALIBRATION

Since AlGaIn/GaN HEMTs are unipolar devices, the hole concentration is very low and does not influence the device characteristics [23]. Thus, the presented models are specially tailored to the electron transport, whereas for the hole transport, conventional models are applied.

A. Low-Field Mobility

The low-field mobility is modeled by an expression similar to that proposed by Caughey and Thomas [22], [24], i.e.,

$$\mu^{LI} = \mu^{\min} + \frac{\mu^L - \mu^{\min}}{1 + (C_I/C^{\text{ref}})^{\alpha}}.$$

C_I denotes the concentration of ionized impurities, μ^L is the mobility in undoped material, and μ^{\min} is the mobility in highly doped material, which is limited by impurity scattering. In order to model the temperature dependence, the mobility values are additionally parameterized using power laws, i.e.,

$$C^{\text{ref}} = C_{300}^{\text{ref}} \left(\frac{T_L}{300 \text{ K}} \right)^{\gamma_0}$$

$$\mu^L = \mu_{300}^L \left(\frac{T_L}{300 \text{ K}} \right)^{\gamma_1}, \quad \mu^{\min} = \mu_{300}^{\min} \left(\frac{T_L}{300 \text{ K}} \right)^{\gamma_2}.$$

μ^L and μ^{\min} are the maximum and the minimum mobility, respectively, and C^{ref} and α are the parameters that describe the mobility decrease with rising impurity concentration. Our model assumes the high mobility consistent with the high-quality substrates of the simulated devices. A profound discussion on the choice of the parameters describing the temperature dependence (γ_0 , γ_1 , and γ_2) based on experimental data from measurements at elevated ambient temperature can be found in [25]. The values used for the low-field mobility in the simulations are listed in Table I.

B. High-Field Mobility

The models proposed for the high-field mobility are based on the mobility expression of the form [26]

$$\mu(E) = \frac{\mu^{LI}}{\xi + \left((1 - \xi)^{\beta} + \left(\frac{\mu^{LI} E}{v_{\text{sat}}} \right)^{\beta} \right)^{1/\beta}}. \quad (1)$$

μ^{LI} is the low-field electron mobility as previously calculated, v_{sat} is the electron saturation velocity, and E is the electric field. The same expression with different values for ξ and β was used by [27].

In order to obtain a consistent HD mobility expression, the local energy balance equation

$$E^2 \mu = \frac{3k_B \Delta T_n}{2q\tau_e} \quad (2)$$

is solved for $E(T_n)$, which is then inserted into (1). This is performed with $\xi = 1/2$ for both models and with $\beta = 2$ and $\beta = 1$ for the first and the second model, respectively. T_n is the electron temperature, and τ_e is the electron energy relaxation time.

a) *Model 1*: The expression obtained with the chosen values for ξ and β is identical with the one proposed by Hänsch *et al.* [28]. In order to account for NDM effects, it is modified by introducing two parameters (γ_3 and γ_4). Thus

$$\mu(T_n) = \frac{\mu^{LI} (T_n/T_L)^{\gamma_3}}{(1 + \alpha^{1/\gamma_4})^{\gamma_4}}$$

$$\alpha = \frac{3k_B \mu^{LI} (T_n - T_L)}{2q\tau_e (v_f)^2}.$$

In the standard Hänsch model, v_f corresponds to saturation velocity v_{sat} as in (1). However, due to the powered temperature term $(T_n/T_L)^{\gamma_3}$ in the numerator, the velocity is steadily decreasing at high fields. Hence, v_f does not describe the saturation velocity as a physical quantity, although it does affect the high-field transport characteristics. τ_e is the energy relaxation time, which is calculated using the following model depending on the carrier energy:

$$\tau_e = \tau_{e,0} + \tau_{e,1} \left(\frac{T_n}{300 \text{ K}} \right)$$

with $\tau_{e,0} = 0.021$ ps and $\tau_{e,1} = 0.004$ ps. The parameter γ_4 has a more pronounced effect at low fields, whereas γ_3 primarily influences the high-field mobility, although their impact cannot be isolated to a specific field region. The conventional Hänsch model corresponds to the parameter set $\gamma_3 = 0$, $\gamma_4 = 1$; however, in order to approximate the simulation and experimental data, a set with $\gamma_3 = -0.3$ and $\gamma_4 = 2.4$ is chosen. Fig. 1 shows the velocity-field characteristics obtained for the model compared against results from bulk material measurements [29], two-dimensional electron gas (2DEG) experiments [30], and own single-particle MC simulation results [31].

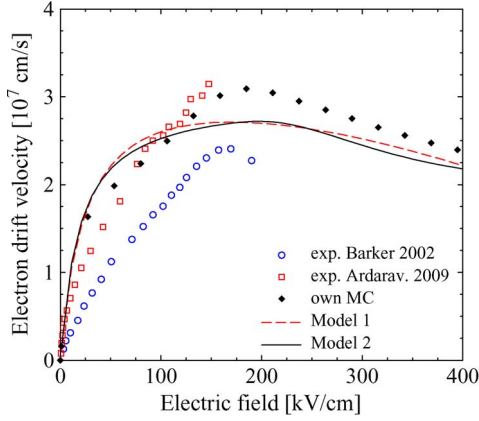


Fig. 1. Electron drift velocity versus electric field: simulations with different mobility models compared with MC simulation results and experimental data.

b) Model 2: Inserting (2) into (1) with $\xi = 1/2$ and $\beta = 1$ gives the following expressions for the high-field mobility:

$$\begin{aligned}\mu_{\Gamma}(T_n) &= \frac{2\mu_{\Gamma}^{LI}}{2 + \alpha_{\Gamma} + \sqrt{\alpha_{\Gamma}(4 + \alpha_{\Gamma})}} \\ \alpha_{\Gamma} &= \frac{3k_B\mu_{\Gamma}^{LI}(T_n - T_L)}{2q\tau_{\Gamma}(v_{f,\Gamma})^2} \\ \mu_U(T_n) &= \frac{2\mu_U^{LI}}{2 + \alpha_U + \sqrt{\alpha_U(4 + \alpha_U)}} \\ \alpha_U &= \frac{3k_B\mu_U^{LI}(T_n - T_L)}{2q\tau_U(v_{f,U})^2}.\end{aligned}$$

Here, $\mu_{\Gamma}(T_n)$ describes the mobility in the lowest conduction valley and $\mu_U(T_n)$ in the higher valleys. In order to approximate the intervalley transfer at high fields, a weighted mean is built. Thus

$$\mu(T_n) = \frac{\mu_{\Gamma}(T_n) + \mu_U(T_n)P_{HD}(T_n)}{1 + P_{HD}(T_n)}. \quad (3)$$

$P_{HD}(T_n)$ is the valley occupancy [32], i.e.,

$$P_{HD}(T_n) = \frac{M_U}{M_{\Gamma}} \left(\frac{m_U^*}{m_{\Gamma}^*} \right)^{3/2} \exp \left(-\frac{\Delta E_C}{k_B T_n} \right)$$

where m_{Γ}^* and m_U^* are the electron masses in the Γ and U valleys, respectively (M is the number of equivalent valleys), and ΔE_C is the difference in the conduction bands. Fig. 2 compares the valley occupancy as a function of the electric field as calculated in the model and MC simulation. Since all MC simulations and experiments, on which we rely to calibrate the low-field mobility, were performed at low electric fields, we set $\mu_{\Gamma} = \mu^{LI}$ as calculated by the low-field mobility model. Using a down-scaled mobility ($\mu_U = 0.1 \times \mu^{LI}$ supported by MC data), velocity parameter (v_f), and up-scaled energy relaxation time ($\tau_U = 8 \times \tau_{\epsilon}$) in the higher band results in a decrease in the electron velocity at higher fields. The parameters for this model are summarized in Table II.

The two-valley approach delivers a good approximation not only to the MC simulation results but also to Model 1 (see Fig. 1). It is a carefully chosen tradeoff between a match with

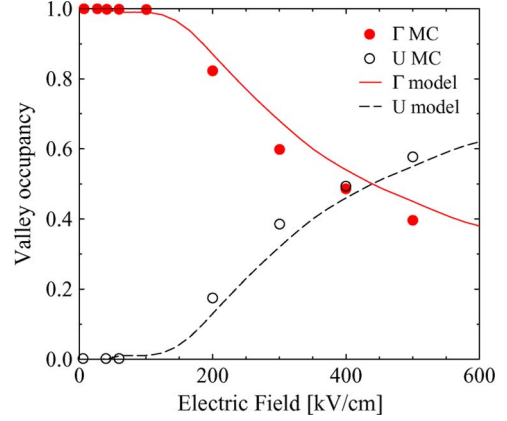


Fig. 2. Valley occupancy as a function of the electric field.

TABLE II
HIGH-FIELD MOBILITY PARAMETERS

| μ_{Γ}/μ^{LI} | μ_U/μ^{LI} | $v_{f,\Gamma}$ | $v_{f,U}$ | τ_{Γ} | τ_U | ΔE_C | m_U^*/m_{Γ}^* | M_U/M_{Γ} |
|-------------------------|------------------|-----------------|-----------------|-------------------|-------------------|--------------|----------------------|------------------|
| | | [cm/s] | [cm/s] | τ_{ϵ} | τ_{ϵ} | [eV] | | |
| 1.0 | 0.1 | 3×10^7 | 1×10^7 | 1.0 | 8.0 | 1.4 | 1.5 | 6.0 |

the MC simulation results on the one hand and calculation complexity and convergence behavior on the other hand. Whereas the models deliver consistent results, the two approaches expose some differences. Model 1 is close to already established models and offers a straightforward calibration with only two auxiliary parameters (within a narrow value range). Model 2 is more complex; however, it allows for a more flexible calibration. The parameters are derived from physical quantities.

The models are to be used for submicrometer devices. However, for large devices, a DD model is sufficient while requiring a lower computational effort. Based on Model 2, a corresponding DD model can be easily synthesized. From (1) and $\xi = 1/2$ and $\beta = 1$ (the same set as in Model 2) again two sets of $\mu(E)$ are calculated. The weighted mean is built corresponding to (3) but with an occupancy $P_{DD}(E)$ as follows (ΔE_C is the difference in conduction bands):

$$P_{DD}(E) = \frac{M_U}{M_{\Gamma}} \left(\frac{m_U^*}{m_{\Gamma}^*} \right)^{3/2} \exp \left(-\frac{\Delta E_C}{k_B T_L \left(1 + \frac{E}{E_0} \right)} \right).$$

All of the proposed models are suitable for implementation in technology computer-aided design tools.

III. SIMULATION SETUP

For good control of the sheet carrier concentration in the 2DEG, the alloy composition and the abruptness of the AlGaIn/GaN interface has to be determined. Various methods such as high-resolution X-ray diffraction, transmission electron microscopy, and elastic recoil detection have been used [33]–[35]. A good estimate of the effective channel thickness of the conducting region is required for the simulator. The nominal value for the thickness of the 2DEG region has been given in the literature to be in the order of 2–3 nm (see for example [36]), depending on the Al mole fraction in the AlGaIn layer. However,

TABLE III
INTERFACE CHARGE DENSITIES [cm^{-2}]

| | Device A | Device B | Device C |
|-----------------|-----------------------|-----------------------|------------------------|
| channel/barrier | 1.14×10^{13} | 1.22×10^{13} | 0.94×10^{13} |
| barrier/cap | -0.4×10^{13} | -0.4×10^{13} | -0.25×10^{13} |
| cap/passivation | -0.4×10^{13} | -0.4×10^{13} | -0.4×10^{13} |

the effective thickness of the conducting region may be wider than the 2DEG, albeit with a lower density. For the purpose of calibrating the simulator to produce the same current density as in the measured devices, various effective thicknesses of the defect-free conducting GaN layer were analyzed. A value of 50 nm was used in all simulations presented in this work. We further assess the impact of thermionic emission that critically determines the current transport across the heterojunctions. Self-heating effects are accounted for by the lattice heat flow equation. A value of 1.0 eV is used for the work-function energy difference of the gate Schottky contact, supported by experimental results.

IV. DEVICE DESCRIPTION

The AlGaIn/GaN HEMT technology is based on multiwafer metal-oxide chemical vapor deposition growth on 3" semi-insulating SiC substrates. The gate is e-beam defined with different gate lengths ($l_g = 0.25, 0.5, \text{ and } 0.6 \mu\text{m}$). Device isolation is achieved by mesa isolation. An $\text{Al}_x\text{Ga}_{1-x}\text{N}/\text{GaN}$ heterointerface is grown on top of a thick insulating GaN buffer. All layers are unintentionally doped except for the supply layer in some of the devices. We assume a metal diffusion of the metal source and drain contacts reaching into the channel. The positive charge (introduced by polarization effects) at the channel/barrier interface is compensated by a commensurate negative surface charge at the barrier/cap interface. The charge density values for the three devices are listed in Table III. Using the methodology as in [33], theoretical values of $1.7 \times 10^{13} \text{ cm}^{-2}$ and $1.2 \times 10^{13} \text{ cm}^{-2}$ for the $\text{Al}_{0.3}\text{Ga}_{0.7}\text{N}/\text{GaN}$ and $\text{Al}_{0.22}\text{Ga}_{0.78}\text{N}/\text{GaN}$ interfaces, respectively, are calculated. However, in real devices, several effects such as dislocations and surface states reduce the total sheet charge. Thus, lower values are used in the simulations, adopted in order to achieve a 2DEG density similar to the one extracted from Hall measurements.

Devices from three different HEMT generations are measured and simulated: first, a device with field-plate structure (Device A); next, a device with shield-plate structure (Device B); and last, a state-of-the-art device with T-gate (Device C). Layer properties are summarized in Table IV, and the geometry is shown in Fig. 3.

Device A has a gate length $l_g = 0.6 \mu\text{m}$, a field-plate extension length $l_{\text{FP}} = 0.6 \mu\text{m}$, and a gate width $100 \mu\text{m}$. The Al composition in the AlGaIn supply layer is 30%. The latter is δ -doped in order to provide additional carriers and to improve access resistance.

Device B is a $l_g = 0.5 \mu\text{m}$ device featuring a T-shaped gate and a source shield-plate. The $\text{Al}_{0.3}\text{Ga}_{0.7}\text{N}$ barrier layer is also δ -doped.

TABLE IV
LAYER PROPERTIES

| | Device A | Device B | Device C |
|------------------------|----------|----------|----------|
| barrier thickness [nm] | 17 | 17 | 22 |
| Al composition [%] | 30 | 30 | 22 |
| δ doping | yes | yes | no |
| cap thickness [nm] | 5 | 5 | 3 |

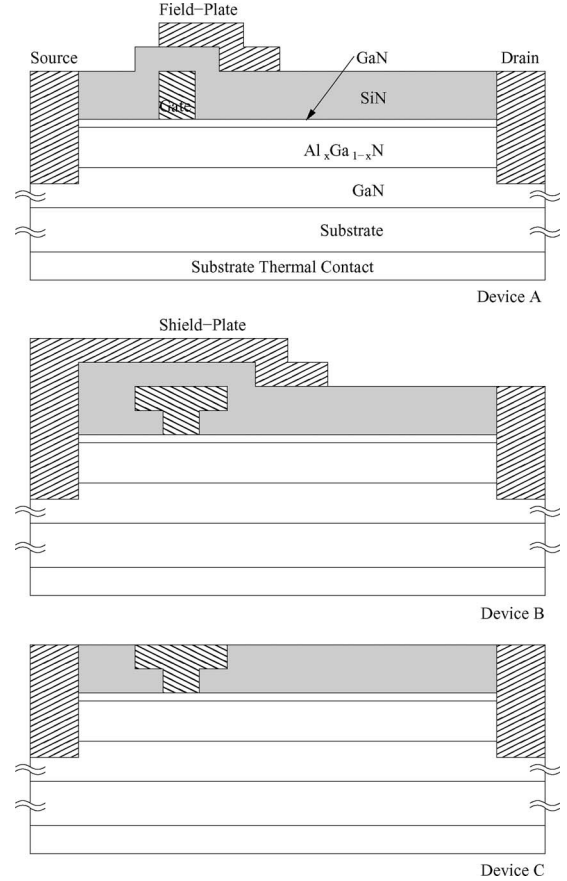


Fig. 3. Schematic layer structure.

The last device has a T-shaped gate with $l_g = 0.25 \mu\text{m}$ and a gate width $W_g = 2 \times 50 \mu\text{m}$ (taken as $1 \times 100 \mu\text{m}$ in the simulations). The Al composition in the supply layer is 22%. Contact resistance of all devices is $0.2 \Omega \cdot \text{mm}$.

V. SIMULATION RESULTS

Using the calibrated setup, the three generations of AlGaIn/GaN-based HEMTs are simulated, and the results are compared with experimental data. In the following sections, the results are discussed.

A. Device A

Fig. 4 compares the measured transfer characteristics ($V_{\text{DS}} = 12 \text{ V}$) with the simulations using the two models. Both setups provide a good agreement. The minor overestimation of the drain current at high gate voltage is due to either gate leakage or real-space transfer [37]. Model 2 delivers a slightly higher

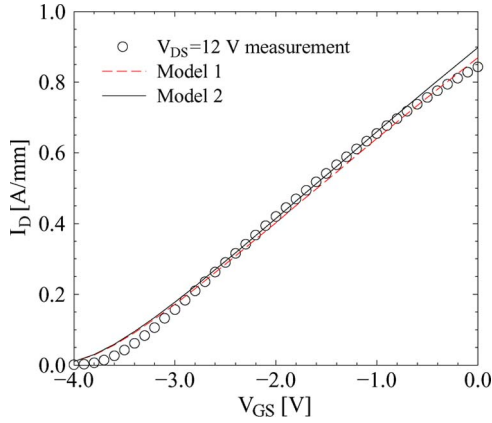


Fig. 4. Comparison of measured transfer characteristics and simulations (Device A).

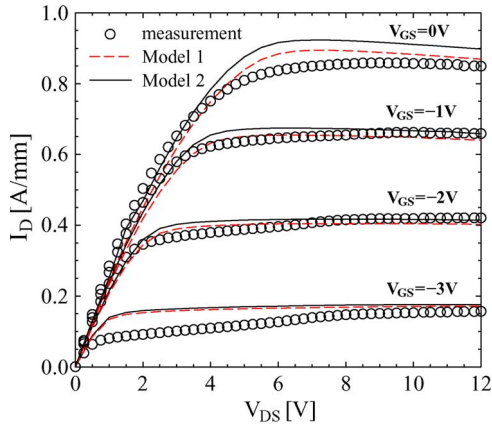


Fig. 5. Comparison of measured output characteristics and simulations (Device A).

gate current. The reason is a small difference in the velocity characteristics at very low electric fields (< 50 kV/cm), which, however, are crucial for the steady-state transport. Fig. 5 shows the output characteristics. Again, an overall good agreement is achieved with a pronounced self-heating effect at high gate voltages.

B. Device B

The transfer characteristics are measured not only at $V_{DS} = 12$ V but also at a higher $V_{DS} = 50$ V. Fig. 6 compares the experiment with simulations, where the results agree very well. The respective output data are provided in Fig. 7.

C. Device C

Fig. 8 compares the measured transfer characteristics at $V_{DS} = 7$ V with simulations. The results achieved with Model 1 match slightly better; however, the model delivers a lower current at low V_{DS} than the measured (see Fig. 9). One possible reason is a higher electron velocity at lower fields in the real device due to low dislocation scattering effects.

AC simulations are performed to compare the theoretical and experimental figures of merit, e.g., cutoff and maximum oscillation frequency (both the measured and simulated frequencies

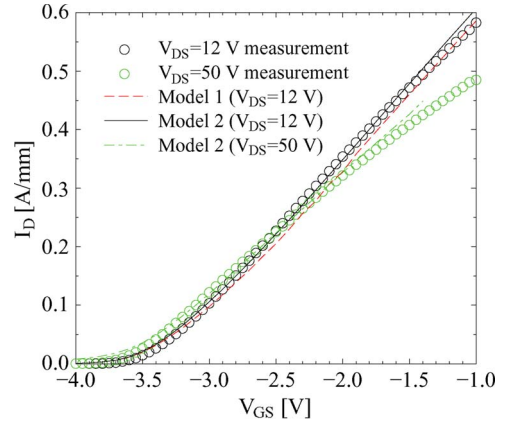


Fig. 6. Comparison of measured transfer characteristics and simulations (Device B).

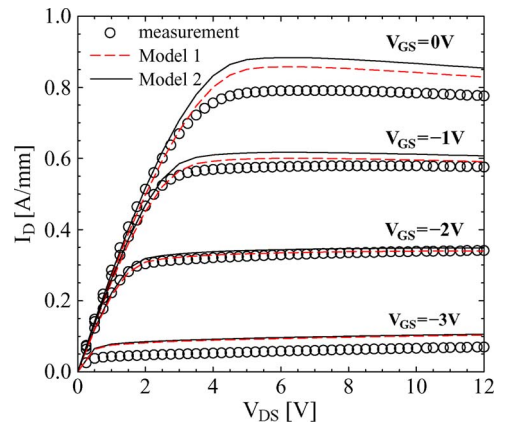


Fig. 7. Comparison of measured output characteristics and simulations (Device B).

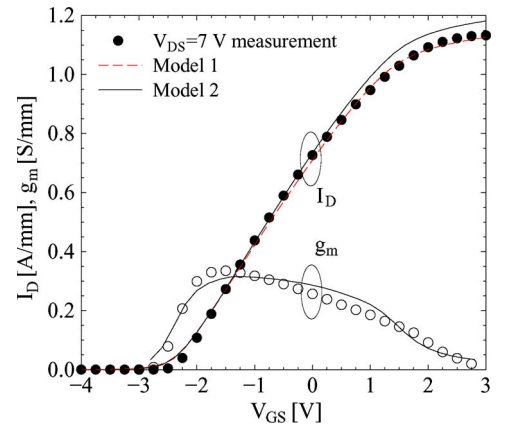


Fig. 8. Comparison of measured transfer characteristics and simulations (Device C).

have been calculated using the established formulas). Fig. 10 shows the measured and simulated cutoff frequency f_T (again at $V_{DS} = 7$ V). In order to account for the parasitics introduced by the measurement equipment, the intrinsic parameters obtained in the simulation are transformed using a standard two-port pad parasitic equivalent circuit [38]. Both models provide a very good agreement with the experiment.

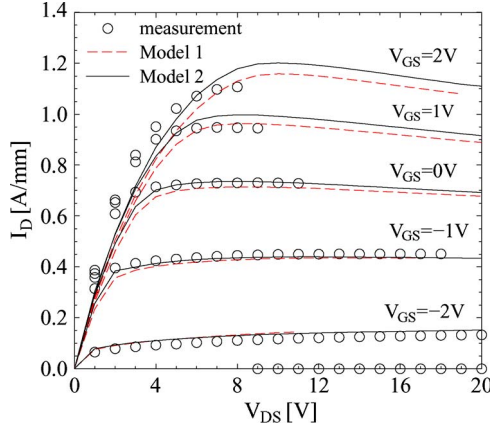


Fig. 9. Comparison of measured output characteristics and simulations (Device C).

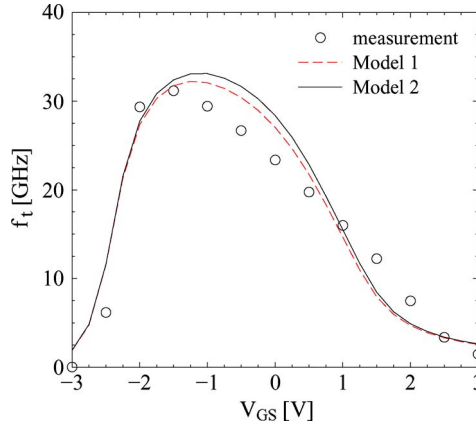


Fig. 10. Comparison of measured cutoff frequency and simulations (Device C).

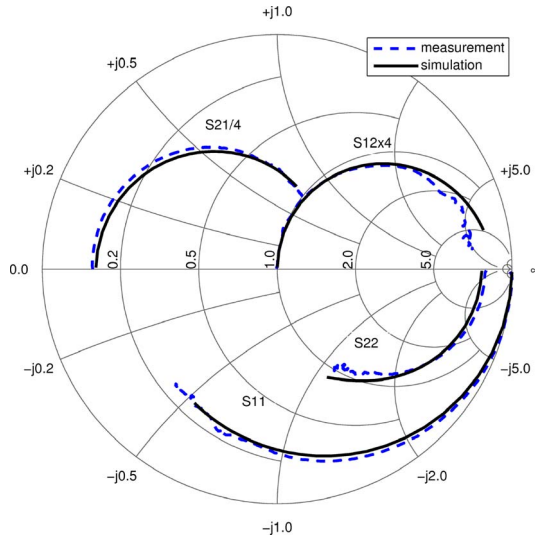


Fig. 11. Simulated S -parameters compared with measured data (Device C).

Fig. 11 compares the measured and simulated (using Model 2) extrinsic S -parameters at $V_{GS} = -1.5$ V and $V_{DS} = 7$ V. An excellent agreement is achieved for all parameters in the frequency range 100 MHz–26 GHz.

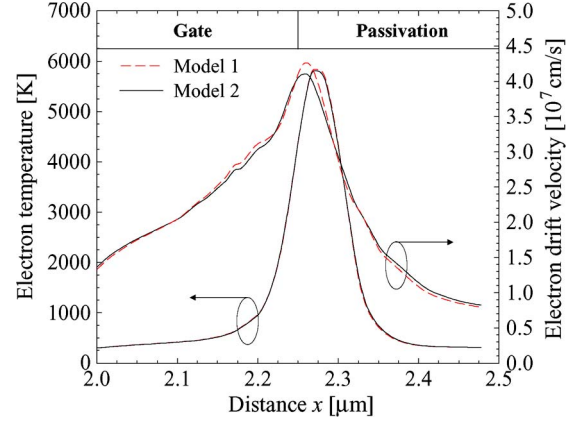


Fig. 12. Simulated electron temperature and velocity along the channel.

The electron transport in the channel under the gate is studied at the same bias point. As the electric field reaches its maximum under the drain side of the gate [39], the peak of the electron temperature is also found there (the gate edge is at $2.25 \mu\text{m}$ in Fig. 12). Consequently, in the same region, a pronounced velocity overshoot effect is observed. The temperature and velocity profiles obtained using both models do not significantly differ.

VI. TRANSCONDUCTANCE COLLAPSE STUDY

As Fig. 8 shows, a good agreement between the measured and simulated transfer characteristics and transconductance (in the rest of the work, only Model 2 is used) is achieved without any changes in the models or model parameters. The simulated transconductance exhibits roughly the same maximum value as the measurement and adequately follows the decrease at higher gate voltage. In order to gain a better understanding of the carrier transport process in the device, the transconductance can be expressed as

$$g_m = \frac{\Delta I_D}{\Delta V_{GS}} = \left(\frac{\Delta n}{\Delta V_{GS}} \right) ev + \left(\frac{\Delta v}{\Delta V_{GS}} \right) ne. \quad (4)$$

The first term describes the contribution of the change in carrier concentration Δn (e is the electron charge). Our simulations show that it is substantial in the gate region, as in the source–gate and gate–drain areas, only a minor variation of the carrier concentration with V_{GS} is observed. The rapid increase in concentration in the bias range near the maximum transconductance combined with a high-electron velocity (see Fig. 13) indeed results in the contribution of this term to the overall g_m .

The second term in (4) involves the change in carrier velocity Δv . Fig. 13 shows the velocity along the channel of the device for V_{GS} between -4 and 3 V (gate is from $x = 2.0 \mu\text{m}$ to $x = 2.25 \mu\text{m}$). There are two distinguishable regions: the extrinsic source–gate region and the intrinsic effective gate region ($l_{G,\text{eff}}$). The latter exhibits a high velocity up to $V_{GS} = -1$ V, which then abruptly decreases. This is to be entirely attributed to the electric field profile, which is depicted in Fig. 14. The complex form at low V_{GS} is due to the negative differential velocity at high electric fields, for which our model accounts.

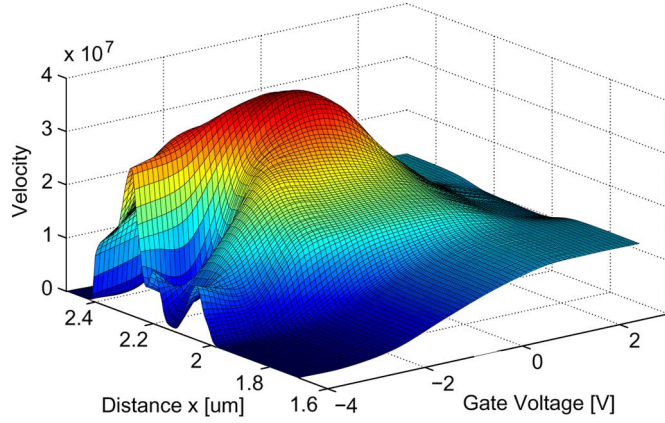


Fig. 13. Electron velocity along the channel [cm/s].

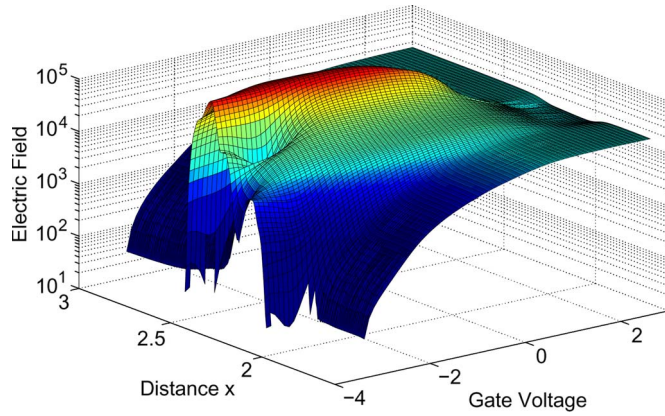
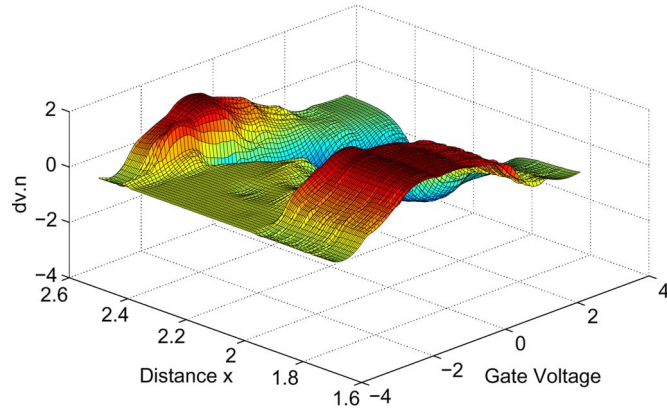


Fig. 14. Electric field along the channel [V/cm].

Fig. 15. Δvn (scaled) along the channel [$1/\text{cm}^2 \cdot \text{s}$].

As the channel under the gate is depleted at this bias, there is no notable effect on the dc characteristics of the device, as shown in Fig. 15, depicting a flat distribution of the product Δvn in the intrinsic region.

In the extrinsic source–gate region, a steady increase in the velocity is observed for V_{GS} between -3 and 0 V, which corresponds to the increase in the electric field. Notably, the electron velocity is very low for $V_{GS} < -3$ V and almost constant for $V_{GS} > 1$ V. The resulting product Δvn shows a distribution that is very similar in form to the transconductance characteristics.

Based on those observations, several conclusions are drawn. The electron velocity at low electric fields in the source–gate region has the highest impact on the transconductance. This is in agreement with the results of Palacios *et al.* [14], who attribute the transconductance decay to a quasi-saturation of the electron velocity (as opposed to the study of Wu *et al.* [13], who attribute it to nonlinearity in the low-field velocity-field characteristics). Our simulations also show that velocity quasi-saturation is the reason for the transconductance decay. However, there are two possible causes for this velocity saturation: increase in the electric field beyond the maximum velocity value [14] or a saturation of the electric field (i.e., constant electric field above a given gate voltage). Given the results demonstrated in Fig. 14, we believe that the latter occurs. We further observe that, at high gate bias ($V_{GS} > 0$ V in the particular structure), the electric field further suppresses the velocity under the gate (see Fig. 15) and causes the secondary collapse of the transconductance.

Our investigation shows that, while important, the velocity-field characteristics are not decisive for the transconductance collapse. As its origin is the electric field distribution and not the material properties, it can be mitigated by optimization as shown in [14] and [40].

VII. CONCLUSION

We propose comprehensive mobility models accounting for the specifics of electron transport in the GaN material system. They are implemented in a device simulator, and simulations of three different HEMT generations are conducted. The presented technology computer-aided design methodology allows the design of next-generation GaN HEMTs through predictive simulations with a good accuracy at reasonable computational cost. We further study the transconductance collapse in GaN-based HEMTs. The main reasons are found to be the electron velocity quasi-saturation due to the electric field profile in the source–gate region and the velocity decrease under the gate. The possibility to tailor the device transconductance gives a novel approach to effectively improve device linearity.

ACKNOWLEDGMENT

The authors would like to thank J. Kuzmik for the fruitful discussions.

REFERENCES

- [1] Y.-F. Wu, B. Keller, P. Fini, S. Keller, T. Jenkins, L. Kehias, S. Denbaars, and U. Mishra, “High Al-content AlGaIn/GaN MODFETs for ultrahigh performance,” *IEEE Electron Device Lett.*, vol. 19, no. 2, pp. 50–53, Feb. 1998.
- [2] Y.-F. Wu, M. Moore, A. Saxler, T. Wisleder, and P. Parikh, “40-W/mm double field-plated GaN HEMTs,” in *Device Research Conf. Digest*, 2006, pp. 151–152.
- [3] N. Sarazin, E. Morvan, M. di Forte Poisson, M. Oualli, C. Gaquiere, O. Jardel, O. Drisse, M. Tordjman, M. Magis, and S. Delage, “AlInN/AlN/GaN HEMT technology on SiC with 10-W/mm and 50% PAE at 10 GHz,” *IEEE Electron Device Lett.*, vol. 31, no. 1, pp. 11–13, 2010.
- [4] K. Shinohara, I. Milosavljevic, S. Burnham, A. Corrión, P. Hashimoto, D. Wong, M. Hu, C. Butler, A. Schmitz, P. Willadsen, K. Boutros, H. Kazemi, and M. Micovic, “60-nm GaN/AlGaIn DH-HEMTs with $1.0 \Omega \cdot \text{mm}$ R_{on} , 2.0 A/mm I_{dmax} , and 153 GHz f_T ,” in *Device Research Conf. Digest*, 2009, pp. 167–168.

- [5] A. Parker and J. Scott, "Intermodulation nulling in GaAs MESFETs," *Electron. Lett.*, vol. 29, no. 22, pp. 1961–1962, 1993.
- [6] R. Quay, *Gallium Nitride Electronics*. Berlin-Heidelberg: Springer, 2008.
- [7] U. Bhapkar and M. Shur, "Monte Carlo calculation of velocity-field characteristics of wurtzite GaN," *J. Appl. Phys.*, vol. 82, pp. 1649–1655, 1997.
- [8] K. Brennan, E. Bellotti, M. Farahmand, H.-E. Nilsson, P. Ruden, and Y. Zhang, "Monte Carlo simulation of noncubic symmetry semiconducting materials and devices," *IEEE Trans. Electron Devices*, vol. 47, no. 10, pp. 1882–1890, 2000.
- [9] Z. Huang, R. Goldberg, J. Chen, Y. Zheng, D. Mott, and P. Shu, "Direct observation of transferred-electron effect in GaN," *Appl. Phys. Lett.*, vol. 67, no. 19, pp. 2825–2826, Nov. 1995.
- [10] M. Wraback, H. Shen, J. Carrano, C. Collins, J. Campbell, R. Dupuis, M. Schurman, and I. Ferguson, "Time-resolved electroabsorption measurement of the transient electron velocity overshoot in GaN," *Appl. Phys. Lett.*, vol. 79, no. 9, pp. 1303–1305, 2001.
- [11] J. Barker, D. Ferry, D. Koleske, and R. Shul, "Bulk GaN and AlGaIn/GaN heterostructure drift velocity measurements and comparison to theoretical models," *J. Appl. Phys.*, vol. 97, no. 6, p. 063705(5), Jun. 2005.
- [12] O. Yilmazoglu, K. Mutamba, D. Pavlidis, and T. Karaduman, "First observation of bias oscillations in GaN Gunn diodes on GaN substrate," *IEEE Trans. Electron Devices*, vol. 55, no. 6, pp. 1563–1567, Jun. 2008.
- [13] Y. Wu, M. Singh, and J. Singh, "Sources of transconductance collapse in III–V nitrides—Consequences of velocity–field relations and source/gate design," *IEEE Trans. Electron Devices*, vol. 52, no. 6, pp. 1048–1054, 2005.
- [14] T. Palacios, S. Rajan, A. Chakraborty, S. Heikman, S. Keller, S. DenBaars, and U. Mishra, "Influence of the dynamic access resistance in the g_m and f_T linearity of AlGaIn/GaN HEMTs," *IEEE Trans. Electron Devices*, vol. 52, no. 10, pp. 2117–2123, 2005.
- [15] M. Farahmand, C. Garetto, E. Bellotti, K. Brennan, M. Goano, E. Ghillino, G. Ghione, J. Albrecht, and P. Ruden, "Monte Carlo simulation of electron transport in the III-Nitride wurtzite phase materials system: Binaries and ternaries," *IEEE Trans. Electron Devices*, vol. 48, no. 3, pp. 535–542, 2001.
- [16] T. Mnatsakanov, M. Levinstein, L. Pomortseva, S. Yurkov, G. Simin, and M. Khan, "Carrier mobility model for GaN," *Solid-State Electron.*, vol. 47, no. 1, pp. 111–115, 2003.
- [17] F. Schwierz, "An electron mobility model for wurtzite GaN," *Solid-State Electron.*, vol. 49, no. 6, pp. 889–895, 2005.
- [18] V. Turin, "A modified transferred-electron high-field mobility model for GaN devices simulation," *Solid-State Electron.*, vol. 49, no. 10, pp. 1678–1682, 2005.
- [19] E. Faracis and A. Anwar, "AlGaIn/GaN HEMTs: Experiment and simulation of DC characteristics," *Solid-State Electron.*, vol. 50, no. 6, pp. 1051–1056, 2006.
- [20] T. Binder, J. Cervenka, K. Dragosits, A. Gehring, T. Grasser, M. Gritsch, R. Klima, M. Knaipp, H. Kosina, R. Mlekus, V. Palankovski, M. Rottinger, R. Rodriguez-Torres, G. Schrom, S. Selberherr, M. Stockinger, and S. Wagner, *MINIMOS-NT Device and Circuit Simulator, User's Guide, Release 2.0*, Institut für Mikroelektronik, Technische Universität Wien, 2002. [Online]. Available: <http://www.iue.tuwien.ac.at/software/minimos-nt>
- [21] V. Palankovski, R. Quay, and S. Selberherr, "Industrial application of heterostructure device simulation," *IEEE J. Solid-State Circuits*, vol. 36, no. 9, pp. 1365–1370, Sep. 2001.
- [22] V. Palankovski and R. Quay, *Analysis and Simulation of Heterostructure Devices*. New York: Springer, 2004.
- [23] T. Simlinger, H. Brech, T. Grave, and S. Selberherr, "Simulation of submicron double-heterojunction high electron mobility transistors with MINIMOS-NT," *IEEE Trans. Electron Devices*, vol. 44, no. 5, pp. 700–707, 1997.
- [24] D. Caughey and R. Thomas, "Carrier mobilities in silicon empirically related to doping and field," *Proc. IEEE*, vol. 55, no. 12, pp. 2192–2193, 1967.
- [25] S. Vitanov, V. Palankovski, S. Maroldt, and R. Quay, "High-temperature modeling of AlGaIn/GaN HEMTs," *Solid-State Electron.*, vol. 54, no. 10, pp. 1105–1112.
- [26] T. Grasser, H. Kosina, and S. Selberherr, "Consistent comparison of drift-diffusion and hydro-dynamic device simulations," in *Proc. Simulation of Semiconductor Processes and Devices*, 1999, pp. 151–154.
- [27] W. Hänsch and M. Miura-Mattausch, "The hot-electron problem in small semiconductor devices," *J. Appl. Phys.*, vol. 60, no. 2, pp. 650–656, 1986.
- [28] W. Hänsch, M. Orlowski, and W. Weber, "The hot-electron problem in submicron MOSFET," in *Proc. Europ. Solid-State Device Research Conf.*, 1988, pp. 597–606.
- [29] J. Barker, R. Akis, D. Ferry, S. Goodnick, T. Thornton, D. Koleske, A. Wickenden, and R. Henry, "High-field transport studies of GaN," *Physica B*, vol. 314, pp. 39–41, 2002.
- [30] L. Ardaravicius, M. Ramonas, J. Liberis, O. Kiprijanovic, A. Matulionis, J. Xie, M. Wu, J. H. Leach, and H. Morkoc, "Electron drift velocity in lattice-matched AlInN/AlN/GaN channel at high electric fields," *J. Appl. Phys.*, vol. 106, no. 7, p. 073708(5), 2009.
- [31] V. Palankovski, A. Marchlewski, E. Ungersboeck, and S. Selberherr, "Identification of transport parameters for gallium nitride based semiconductor devices," in *Proc. MATHMOD*, 2006, pp. 14–1–14–9.
- [32] S. Sze, *Physics of Semiconductor Devices*, 2nd ed. New York: Wiley, 1981.
- [33] O. Ambacher, B. Foutz, J. Smart, J. Shealy, N. Weimann, K. Chu, M. Murphy, A. Sierakowski, W. Schaff, L. Eastman, R. Dimitrov, A. Mitchell, and M. Stutzmann, "Two-dimensional electron gases induced by spontaneous and piezoelectric polarization in undoped and doped Al-GaN/GaN heterostructures," *J. Appl. Phys.*, vol. 87, no. 1, pp. 334–344, 2000.
- [34] D. Jena, I. Smorchkova, A. Gossard, and U. Mishra, "Electron transport in III-V nitride two-dimensional electron gases," *Phys. stat. sol.(b)*, vol. 228, no. 2, pp. 617–619, 2001.
- [35] I. Smorchkova, C. Elsass, J. Ibbetson, R. Vetury, B. Heying, P. Fini, E. Haus, S. DenBaars, J. Speck, and U. Mishra, "Polarization induced charge and electron mobility in AlGaIn/GaN heterostructures grown by plasma-assisted molecular-beam epitaxy," *J. Appl. Phys.*, vol. 86, no. 8, pp. 4520–4526, 1999.
- [36] B. Jogai, "Influence of surface states on the two-dimensional electron gas in AlGaIn/GaN heterojunction field-effect transistors," *J. Appl. Phys.*, vol. 93, no. 3, pp. 1631–1635, 2003.
- [37] R. Quay, K. Hess, R. Reuter, M. Schlechtweg, T. Grave, V. Palankovski, and S. Selberherr, "Nonlinear electronic transport and device performance of HEMTs," *IEEE Trans. Electron Devices*, vol. 48, no. 2, pp. 210–217, 2001.
- [38] S. Vitanov, "Simulation of high electron mobility transistors," Ph.D. thesis, 2010.
- [39] V. Palankovski, S. Vitanov, and R. Quay, "Field-plate optimization of AlGaIn/GaN HEMTs," in *Tech. Dig. IEEE Compound Semiconductor IC Symp.*, San Antonio, Nov. 2006, pp. 107–110.
- [40] S. Vitanov, V. Palankovski, S. Maroldt, and R. Quay, "Non-linearity of transconductance and source–gate resistance of HEMTs," in *Proc. European Solid-State Device Research Conf. Fringe Poster Session*, Sevilla, Spain, Sep. 2010.



Stanislav Vitanov received the Dipl.Ing. degree in electrical engineering from the Technische Universität München, Germany, in 2005 and the Doctoral degree in technical sciences from Technische Universität Wien, Austria, in 2010.

He joined the Advanced Materials and Device Analysis group at the Technische Universität Wien in 2006. He is currently with Infineon Technologies, Villach, Austria. His scientific interests include modeling and simulation of GaN-based devices.



Vassil Palankovski received the Dipl.Ing. degree in electronics from the Technical University Sofia, Bulgaria, in 1993 and the Doctoral degree in technical sciences from the Technische Universität Wien, Austria, in 2000.

Afterwards, he worked for three years in the telecommunications field. In 1997, he joined the Institut für Mikroelektronik, the Technische Universität Wien, as a Postdoctoral Researcher. In summer 2000, he held a visiting research position at LSI Logic Corporation, Milpitas, CA. In 2004, he joined Infineon Technologies, Villach, Austria, for half a year as a Technology Development Engineer. Having received the highest Austrian award for young scientists (START-Prize), he returned to the Technische Universität Wien in 2005 to establish the Advanced Material and Device Analysis group. In 2008, he was elected a member of the young curia of the Austrian Academy of Sciences. He has authored and coauthored over 100 refereed publications and a monograph in the field of modeling and simulation of advanced semiconductor devices.

Stephan Maroldt received the Dipl.Ing. degree in electrical engineering, with emphasis on microelectronics, from the Technical University Ilmenau, Germany, in 2006. After graduation, he began working on his Ph.D. degree in the nanotechnology group at the Technical University Ilmenau in the field of GaN HFET technology. Since 2008, he has been with the Fraunhofer Institute of Applied Solid-State Physics, Freiburg, Germany, where he has continued working toward the Ph.D. degree.

His major field of research is the design and technology for GaN HFET devices and GaN-based microwave switch-mode amplifier circuits.

Rüdiger Quay received the Diploma degree in physics from the Rheinisch-Westfälische Technische Hochschule, Aachen, Germany, in 1997, the second Diploma degree in economics in 2003, the Doctoral (with honors) degree in technical sciences, and the *venia legendi* in microelectronics from the Technische Universität Wien, Austria, in 2009.

He is currently a Research Engineer with the Fraunhofer Institute of Applied Solid-State Physics, Freiburg, Germany, heading the RF-devices and characterization group. He has authored and coauthored over 100 refereed publications and three monographs.

Dr. Quay is a member of MTT and chairman of MTT-6.

Saad Murad received the B.Sc. (highest class honors) degree in electronic engineering from Mosul University, Mosul, Iraq, and the Ph.D. degree in the field of plasma processing technologies for III–V semiconductors from the Department of Electronic Engineering, Glasgow University, Glasgow, U.K., in 1994.

From 1994 to 1998, he was a Postdoctoral Fellow at the Nano-Electronics Research Center, Glasgow University, working on device and process developments for III–V monolithic microwave integrated circuits (MMICs), also the Manager for the fabrication facilities. From 1998 to 2000, he was with Raytheon Electronic Systems, Essex, U.K. His research interests were device simulation and characterization and process development of MOS devices. In 2000, he joined Philips Semiconductors, Nijmegen, The Netherlands (now NXP Semiconductors), where he worked on pHEMTs device and process developments as well as Epi design for high-voltage and -linearity applications. Since 2007, he has been working for NXP mainly on GaN devices, device simulation, and characterization for high RF power applications. He is currently with Azzuro Semiconductors, Magdeburg, Germany. He has about 50 scientific publications. His interests included fabrication of pHEMTs and HEMTs on GaAs and InP devices for MMICs.

Thomas Rödle was born in Friedrichshafen, Germany, in 1967. He received the Ph.D. degree from the University of Göttingen, Germany, in 1996, working on inelastic light scattering on AlAsGaAs-quantum wells.

After having worked for the semiconductor branch of Siemens on cost reduction programs for front- and back-end operations, he joined Philips Semiconductors, Nijmegen, The Netherlands (now NXP Semiconductors) in 1997. He started his career at Philips in process and device development for radio frequency power amplifiers used in base stations. He is currently acting as a Project Manager for wide bandgap semiconductor technologies at NXP Semiconductors.



Siegfried Selberherr (M'79–SM'84–F'93) was born in Klosterneuburg, Austria, in 1955. He received the M.S. degree in electrical engineering and the Ph.D. degree in technical sciences from the Technische Universität Wien, Austria, in 1978 and 1981, respectively.

Since 1984, he has been holding the “*venia docendi*” on computer-aided design. Since 1988, he has been the Chair Professor of the Institut für Mikroelektronik, Technische Universität Wien. From 1998 to 2005, he was the Dean of the Fakultät für Elektrotechnik und Informationstechnik. His current research interests are modeling and simulation for microelectronics engineering.